

# Simplified Analysis of Nonoverlap Short-Circuited Coil Winding Slip Permanent Magnet Couplers

Petrus J. J. van Wyk, *Student Member, IEEE*, and Maarten J. Kamper, *Senior Member, IEEE*

**Abstract**—In this paper, a simplified analysis technique is introduced to allow the  $dq$  modeling of a nonoverlap, short-circuited coil winding slip permanent magnet (PM) coupler (S-PMC). The proposed technique for predicting the coil currents using a number of static finite-element (FE) solutions takes the effect of, amongst others, mutual coupling between the coils and layers into account. The technique also allows a difference in the currents of top- and bottom-layer coils, if such coil windings are used. This all makes the method particularly attractive for use in the design optimization of the S-PMC. Excellent correlation with measured and transient FE analysis results was found for a 2.2 kW S-PMC prototype with an efficiency of 97% at a rated load.

**Index Terms**—Design optimization,  $dq$ -analysis, finite-element method, slip permanent magnet coupler (S-PMC), wind energy.

## I. INTRODUCTION

MAGNETIC and electromagnetic couplers are used to transfer the torque and power from one mechanical system to another without any mechanical connection. Magnetic couplers are synchronous torque couplers that transfer torque synchronously between mechanical systems by means of the use of permanent magnets (PMs) [1], [2]. Electromagnetic couplers in turn transfer torque by slip speed operation. An example of such a coupler consists of a cage rotor and rotating stator that is converter-fed controlled via slip rings [3]. Another example is the well-known eddy current coupler which is widely used in industry [4], [5]. Another variation of this is the use of a PM-rotor and a short-circuited wound- or cage rotor that operate at slip speed with respect to each other. In this paper, this is called a slip PM coupler (S-PMC), which has received surprisingly little attention in the literature [6]–[9].

In [6] and [9], the uses of S-PMCs are investigated for wind turbine generator applications. In [6], the S-PMC and a PM synchronous generator (PMSG) are combined into a single unit with a common PM rotor, while in [9], the S-PMC and PMSG are separate machines on the same drive train. An extensive design study of different-winding S-PMCs is done in [8], which includes, amongst others, the design of an axial-flux cage winding S-PMC as in [7].

Manuscript received December 14, 2015; revised May 11, 2016; accepted July 9, 2016. Date of publication August 8, 2016; date of current version November 18, 2016. Paper 2015-EMC-1054.R1, presented at the 2015 IEEE International Electric Machines & Drives Conference, Coeur d'Alene, ID, USA, May 10–13, 2015, and approved for publication in the IEEE TRANSACTIONS ON INDUSTRY APPLICATIONS by the Electric Machines Committee of the IEEE Industry Applications Society.

The authors are with the Department of Electrical and Electronic Engineering, Stellenbosch University, Stellenbosch 7600, South Africa (e-mail: petrus.wyk@gmail.com; kamper@sun.ac.za).

Color versions of one or more of the figures in this paper are available online at <http://ieeexplore.ieee.org>.

Digital Object Identifier 10.1109/TIA.2016.2598532

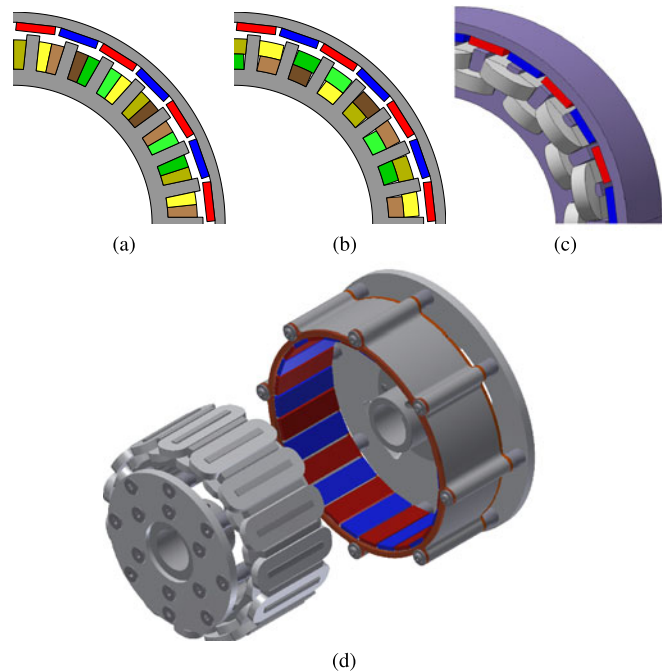


Fig. 1. Slip coupler layouts, with (a) side-by-side layout, (b) top-bottom layout with larger cross sectional area of the top-layer coil (light and dark shades of a color indicates polarities of a coil) and (c) a 3-D representation of (b). A CAD representation of the slip coupler assembly is shown in (d).

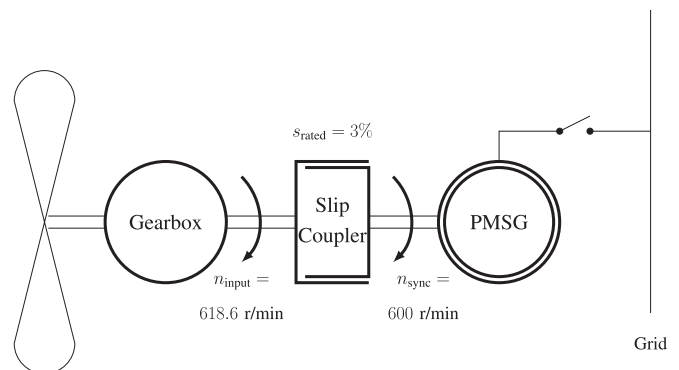


Fig. 2. Illustration of the application of a slip coupler that acts as a coupler between a wind-side gearbox and a grid-connected synchronous generator. The given speeds and slip are rated values.

A double-layer, nonoverlap short-circuited winding S-PMC is introduced in [8], which seems to be a very attractive design due to its simple construction. To simplify the construction, each of the nonoverlap coils is individually short circuited, effectively creating a high phase number machine. Examples of such short-circuited coil layouts are shown in Fig. 1 and can either be

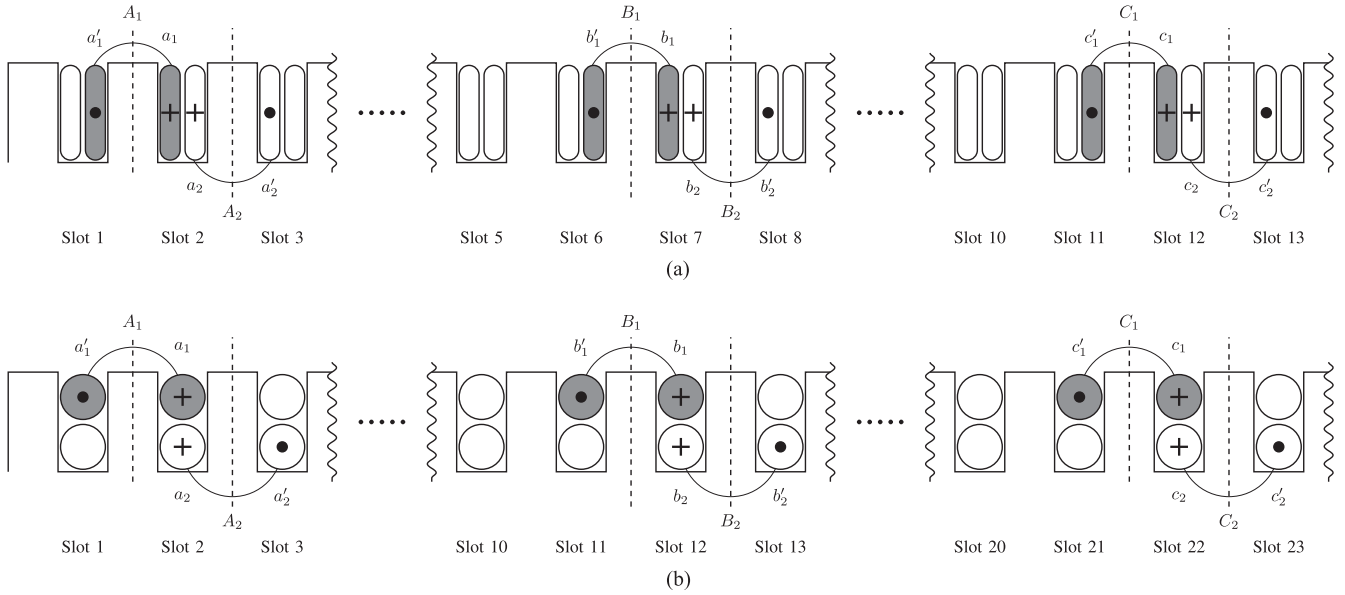


Fig. 3. Double layer winding layout of 28/30 pole/slot combination PM machine, with (a) a side-by-side configuration and (b) a top-and-bottom layer configuration. A three-phase winding set, set  $i = 1$ , is highlighted and given by  $a_1 + a'_1, b_1 + b'_1, c_1 + c'_1$ . For (b) there are five top-layer and five bottom-layer three-phase winding sets.

side-by-side in the slot [see Fig. 1(a)] or top-bottom in the slot [see Fig. 1(b)]. To simplify analysis in the static finite-element (FE) modeling used in [8], it is assumed that the RMS currents in the top and bottom coils of the double layer winding machine are equal, and that groups of adjacent coils are in phase in terms of current. Thus, the machine is in effect analyzed as a normal three-phase machine and is easily modeled in the  $dq$  reference frame. However, this simplification, as shown in [9], can lead to a significant error in the calculating of current and torque and, thus, cannot be used in general for all pole-slot combination nonoverlap coil winding machines.

Hence, the machine designer is presented with a unique problem—how to analyze such a multiphase, double layer winding machine in the  $dq$  reference frame, given that the coil currents are out of phase and potentially of different magnitudes between layers. In the literature regarding the subject of multiphase  $dq$  modeling [10], [11], it is assumed that the RMS currents in the various phases are of equal magnitude, and Clarke's transformation is simply adapted to accommodate the required number of phases. This approach cannot work in cases where the currents differ between the two layers, and additionally the transformation matrix becomes unnecessarily complex for high phase number windings.

In this paper, the attempt is to illustrate a simple technique which enables the  $dq$  modeling of nonoverlap winding S-PMCs where all the tooth coils are separately short circuited. In this technique, time-stepped static FE solutions are used, which are much faster in the design optimization and simulation of the machine than using transient FE simulations. A further aspect that is considered in this paper is the MMF analysis and proof-of-working of the machine with all the coils separately short circuited. As valid three-phase pole-slot combinations are well known, only these pole-slot combinations are considered in the

analysis in this paper, i.e., where the number of nonoverlap short-circuited coils is a multiple of three for double layer windings and a multiple of six for single layer windings.

## II. PM SLIP COUPLER CONCEPT

The S-PMC design used as a case study in this paper is shown in Fig. 1, which is further referred to as a slip coupler. The slip coupler has a 28/30 pole/slot combination, with all 30 coils individually short circuited as shown in Fig. 1(c) and (d), thus implying that the machine has 30 phases. The construction is kept as simple as possible, with a very basic wound rotor slot design and solid aluminum coils. The solid coils can also be replaced with stacks of thin conductor plates, further simplifying the construction and reducing cost. In Fig. 1(a), the cross section of a side-by-side coil layout is shown, while in Fig. 1(b) and (c) the cross section and a three-dimensional (3-D) picture of a top-bottom coil layout are shown, respectively. Both layouts have their advantages and disadvantages. The side-by-side winding has the advantage of lower conductor losses due to its shorter end windings. The top-bottom layout in turn is easier to manufacture and construct if the slots are narrow and deep. Note from the top-bottom winding layout in Fig. 1(b) that the top-layer coils have a larger cross-sectional area than that of the bottom-layer coils. This aspect already indicates that the induced currents in the top and bottom layers will be different.

The slip coupler in this paper is designed for a wind energy application, and acts as a coupler between a gearbox and a synchronous generator. The proposed drive train, consisting of a gearbox, slip coupler, and PMSG, is shown in Fig. 2. The rated output speed is 600 r/min, which is the fixed synchronous speed of the grid-connected PMSG. The slip coupler is rated at a slip of  $s = 3\%$ , which implies an efficiency of 97%. The rated torque is 42 N·m.

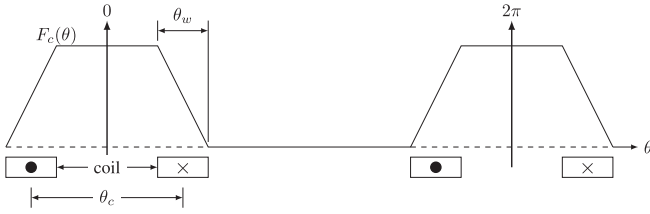


Fig. 4. Wound rotor coil MMF waveform.

### III. PROPOSED ANALYSIS TECHNIQUE

The induced voltages and currents in the short-circuited coils of the slip coupler are assumed in the analysis to be sinusoidal. This is a valid assumption for good winding factor, high pole number nonoverlap-winding PM machines, as is also shown in this paper. With this assumption of considering only fundamental flux components in the analysis the transformation from  $n$ -phase variables to  $dq$  variables becomes simple as only  $\alpha$ - $\beta$  variables have to be considered in the Clarke transformation [10]. With sinusoidal phase-current quantities, it implies in the  $dq$  reference frame that the induced  $dq$  coil currents have  $dc$  quantities.

In the analysis, only valid three-phase nonoverlap pole-slot combinations are considered as these combinations are well known. This leaves the opportunity to divide the number of coils into sets of three-phase coils and use the well-known Park transformation to transform the  $abc$  variables of each set to  $dq$  variables.

Two scenarios exist for the winding configuration of the double layer, nonoverlap winding machine considered, namely, a side-by-side configuration as shown in Fig. 3(a) and a top-bottom layer configuration as shown in Fig. 3(b). To analyze the windings of Fig. 3, the short-circuited phase coils are divided into sets of three-phase coils. For the side-by-side coil winding, the smallest machine section that repeats itself in the machine appears within  $S = 15$  slots, i.e., 15 adjacent phase coils can be divided into  $m = 15/3 = 5$  three-phase coil sets to form a complete winding. The electrical spatial distribution of a set of three phase coils in the side-by-side coil winding is illustrated in Fig. 3(a), where phase-coil axes  $A_1$ ,  $B_1$ , and  $C_1$  of coils 1, 6, and 11 of set  $i = 1$  are  $120^\circ$  out of phase. Note that the subscript  $i$  denotes the set number of a given set of three-phase coils, with  $i = 1, 2, \dots, m$ .

For the top-bottom coil winding of Fig. 3(b), the top and bottom coil layers have to be considered separately as the RMS currents of these layers are not necessarily the same. In this case, the machine section of a layer can now only be found over  $S = 30$  slots of the machine. As shown in Fig. 3(b) for set  $i = 1$ , coils 1, 11, and 21 of the top-layer form a three-phase coil set. For the top-bottom coil winding, thus,  $i = i_U = 1, 3, \dots, 9$  are the top-layer coil sets, while  $i = i_L = 2, 4, \dots, 10$  are the bottom-layer coil sets.

Grouping the coil windings in this way enables the interpretation of the machine as  $m$  sets (for the side-by-side winding) or  $2 \times m$  sets (for the top-bottom winding) of balanced three-

phase quantities (current or flux linkage). The three-phase quantities of these sets are then all separately transformed to the  $dq$  reference frame, giving  $m$  sets or  $2 \times m$  sets of  $dq$  quantities. These  $dq$  sets are analyzed separately in exactly the same way that a normal three-phase machine is analyzed, and a torque value is calculated for each set. The generated torques of the sets are then summed to give the total torque of the machine.

This method is advantageous in that it is relatively simple. However, there are two aspects that need further investigation. The first aspect is to prove that the short-circuited coil winding layout indeed generates the correct rotating working harmonic MMF, and to determine and evaluate the harmonic content of the airgap MMF. This aspect is dealt with in the next section. The second aspect is to consider the mutual coupling between the  $m$ -sets of three-phase windings and to determine if this is taken into account correctly in the analysis. This aspect is dealt with in Sections V and VII.

### IV. WOUND ROTOR MMF

The wound rotor MMF generated by a coil is assumed to be represented by the waveform of Fig. 4, which allows for the fact that the MMF does not change abruptly at each coil side. It can be shown that the MMF of Fig. 4 can be expressed for the  $n$ th MMF harmonic as [12]

$$F_{cn} = \frac{2}{\pi|n|} k_{pn} \xi_n i_c \cos(n\theta) \quad (1)$$

where  $i_c$  is the coil current and  $k_{pn}$  and  $\xi_n$  are the coil pitch and coil side-width factors given by

$$k_{pn} = \sin(n\theta_c/2) \quad \text{and} \quad \xi_n = \frac{\sin(|n|\theta_w/2)}{|n|\theta_w/2} \quad (2)$$

with the electrical angles  $\theta_c$  and  $\theta_w$  as defined in Fig. 4. As before, we can group a set,  $i$ , of three coils of which the induced coil currents are  $120^\circ$  out of phase [e.g., coils 1, 6, and 11 of the side-by-side coil winding of Fig. 3(a)], to generate a three-phase MMF that can be expressed from (1) as

$$F_{in} = \frac{3}{\pi|n|} k_{pn} \xi_n I \sin(\alpha_i + \beta_i) \quad (3)$$

where  $I$  is the amplitude of the sinusoidal coil currents and [12]

$$\begin{aligned} \alpha_i &= \omega t - (i-1)\theta_t \quad \text{with} \quad \theta_t = p\pi/N_s \\ \beta_i &= n[\theta - (i-1)\theta_s] \quad \text{with} \quad \theta_s = 2\pi/S \\ n &= 3k - 1, \quad k \in \mathbb{Z}. \end{aligned} \quad (4)$$

In (4),  $\theta_t$  is the phase angle between the currents of adjacent coils,  $\theta_s$  is the electrical slot pitch angle,  $p$  is the number of poles,  $N_s$  is the number of rotor slots, and  $S$  is the number of rotor slots per machine section that repeats itself in the machine. Note from Figs. 3 and 4 that  $\theta_c = \theta_s$  for the top-and-bottom coil winding, but  $\theta_c < \theta_s$  for the side-by-side coil winding.

#### A. Side-by-Side Nonoverlap Winding

For the side-by-side winding of Fig. 3(a) with  $S = 15$  and  $i = 1, 2, \dots, m$  ( $m = 5$  in this case) three-phase coil sets, (3)

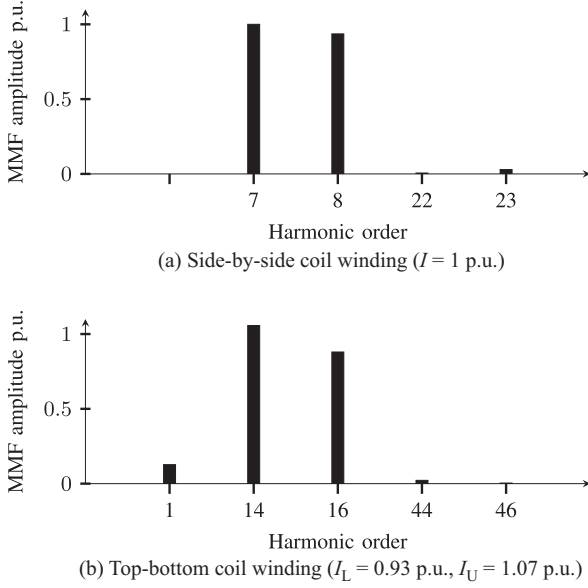


Fig. 5. Per-unit MMF Harmonics (per unit values are calculated with the working harmonic of the side-by-side winding as the base value).

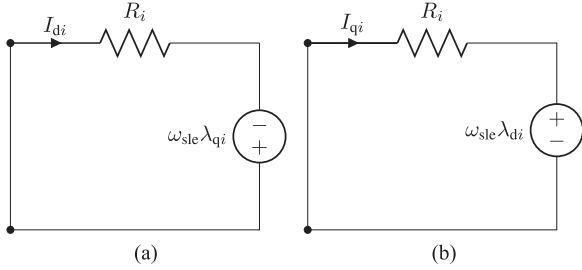


Fig. 6. Steady-state equivalent circuits of the (a)  $d$ -axis and (b)  $q$ -axis of the  $i$ th three-phase coil set.

can be used to obtain a mathematical expression for the wound rotor MMF of the complete multi three-phase side-by-side coil winding as

$$\begin{aligned}
 F_{sn} &= \frac{3}{\pi|n|} k_{pn} \xi_n \sum_{i=1}^m I \sin(\alpha_i + \beta_i) \\
 &= \frac{3m}{\pi|n|} k_{pn} \xi_n I \sin(\omega t + n\theta) \\
 [n &= -7, 8, -22, 23, -37, 38, \dots]. \quad (5)
 \end{aligned}$$

The sign of the harmonics in (5) indicates the traveling direction of the harmonic wave. Note for all other harmonics besides those given in (5) that the rotor MMF is zero. The latter is interesting as  $|n| = 7$  is the working harmonic (which can be understood from the machine section of Fig. 1(a) which has seven magnet pole pairs) of this winding, which implies there are no sub rotor-MMF harmonics generated by this  $5 \times 3$ -phase coil winding; usually nonoverlap three-phase windings have relatively large sub-MMF harmonics [13], [14]. The per-unit amplitudes of the MMF harmonics of (5) are given in Fig. 5(a).

### B. Top-and-Bottom Layer Nonoverlap Winding

Using (3) and (4) for the top-bottom coil winding of Fig. 3(b) with  $m = 5$  for both the top and bottom layers and  $S = 30$ , the rotor MMF for the complete winding is expressed as

$$\begin{aligned}
 F_{sn} &= \frac{3}{\pi|n|} k_{pn} \xi_n \left[ \sum_{i=i_L} I_L \sin(\alpha_i + \beta_i) \right. \\
 &\quad \left. + \sum_{i=i_U} I_U \sin(\alpha_i + \beta_i) \right] \\
 &\quad \{i_U = 1, 3, \dots, 9 \quad \text{and} \quad i_L = 2, 4, \dots, 10\} \\
 &= \frac{3m}{\pi|n|} k_{pn} \xi_n \left[ I_L \sin(\omega t + n\theta) \right. \\
 &\quad \left. + I_U \sin[(\omega t - \theta_t) + n(\theta - \theta_s)] \right] \\
 [n &= 1, -14, 16, -44, 46, -74, 76, \dots]. \quad (6)
 \end{aligned}$$

The working MMF harmonic in this case is  $|n| = 14$ , which corresponds with the 14 pole pairs in the machine section considered for the top-bottom winding. In (6), it is shown that the top-bottom winding generates a sub working-harmonic  $|n| = 1$ , but this becomes zero if  $I_L = I_U$  and the top and bottom MMFs cancel each other in (6). The per unit amplitudes of the MMF harmonics of the top-bottom winding are given in Fig. 5(b). These harmonics are calculated with a typical difference in the top and bottom coil currents  $I_U$  and  $I_L$  as given in Fig. 5(b). From this, it is clear that the subworking harmonic is still very small for the top-bottom winding. In general, the harmonic content for both the side-by-side and top-bottom windings is shown to be relatively small.

## V. MODELING

In Fig. 6, the short-circuited steady-state  $dq$ -equivalent circuits of the  $i$ th set of three-phase coils of the wound rotor of the slip coupler are shown. Using these  $dq$ -equivalent circuits the steady-state  $dq$ -equations (motor reference with positive current flowing into the machine) can be written as

$$0 = R_i I_{di} - \omega_{sle} \lambda_{qi} \quad (7)$$

$$0 = R_i I_{qi} + \omega_{sle} \lambda_{di} \quad (8)$$

where  $I_{di}$  and  $I_{qi}$  are the wound rotor  $d$ - and  $q$ -axis currents, respectively.  $\lambda_{di}$  and  $\lambda_{qi}$  are the  $dq$  flux linkages.  $R_i$  is the per phase winding resistance.  $\omega_{sle}$  is the electrical slip speed, which is defined as  $\omega_{sle} = \omega_{PM} - \omega_R$ , with  $\omega_{PM}$  being the input PM-rotor speed and  $\omega_R$  being the output wound-rotor speed, both in electrical rad/s.

### A. Side-by-Side Coil Winding

When considering the side-by-side coil winding configuration, the RMS phase currents are the same across all phase coils. The  $d$ - and  $q$ -axis currents are thus the same, with  $I_{d1} = I_{d2} = \dots = I_{dm}$  and  $I_{q1} = I_{q2} = \dots = I_{qm}$ .

The  $dq$  inductances must be defined and must include mutual inductance between the different  $dq_i$  circuits. Evaluating on the  $d$ -axis for  $i = 1$ , the flux linkage can be written as

$$\lambda_{d1} = L_{d(1,1)}I_{d1} + L_{d(1,2)}I_{d2} + \dots + L_{d(1,m)}I_{dm} + \lambda_{m1} \quad (9)$$

where  $L_{d(1,1)}$  is the circuit's self-inductance and  $L_{d(1,2)}$  to  $L_{d(1,m)}$  are mutual inductances between circuit  $i = 1$  and circuits  $i = 2$  to  $m$ .  $\lambda_{m1}$  is the PM flux linkage contribution. Since all  $d$ -axis currents are the same (9) is reduced to

$$\lambda_{d1} = L_{d1}I_{d1} + \lambda_{m1} \quad (10)$$

where  $L_{d1}$  is the total (self and mutual) inductance of set  $i = 1$ . In exactly the same way, it can be shown that the  $q$ -axis flux linkage for set  $i = 1$  is

$$\lambda_{q1} = L_{q1}I_{q1}. \quad (11)$$

### B. Top–Bottom Layer Configuration

To analyze the top–bottom coil winding configuration, the top and bottom layers are considered separately as before with  $m = 5$  sets in the top layer and  $m = 5$  sets in the bottom layer. The top layer sets are numbered  $i = i_U = 1, 3, \dots, 9$  and the bottom-layer sets  $i = i_L = 2, 4, \dots, 10$ . The top-layer phases have identical RMS phase currents, and thus, the  $dq$  currents are also the same. The top-layer  $dq$  currents are written as

$$I_{d1} = I_{d3} = I_{d5} = I_{d7} = I_{d9} = I_{dU} \quad (12)$$

$$I_{q1} = I_{q3} = I_{q5} = I_{q7} = I_{q9} = I_{qU}. \quad (13)$$

Similarly, the bottom-layer  $dq$  currents are written as

$$I_{d2} = I_{d4} = I_{d6} = I_{d8} = I_{d10} = I_{dL} \quad (14)$$

$$I_{q2} = I_{q4} = I_{q6} = I_{q8} = I_{q10} = I_{qL}. \quad (15)$$

Using (12) and (14), (9) is written for the  $d$ -axis flux linkage of the top-layer set  $i = 1$  as

$$\begin{aligned} \lambda_{d1} &= (L_{d(1,1)} + L_{d(1,3)} + \dots + L_{d(1,9)})I_{dU} \\ &\quad + (L_{d(1,2)} + L_{d(1,4)} + \dots + L_{d(1,10)})I_{dL} + \lambda_{m1} \\ &= L_{d1U}I_{dU} + L_{d1L}I_{dL} + \lambda_{m1} \end{aligned} \quad (16)$$

where  $L_{d1U}$  is the total  $d$ -axis inductance of top-layer coil set  $i = 1$  and  $L_{d1L}$  is the  $d$ -axis mutual inductance of coil set  $i = 1$  with the bottom-layer coil sets. Note that  $L_{d1U}$  is the inductance contribution of all the coils in the top layer, including the self-inductance ( $L_{d(1,1)}$ ) of set  $i = 1$ . Applying this in the same way to the  $q$ -axis, the  $q$ -axis flux linkage is written as

$$\lambda_{q1} = L_{q1U}I_{qU} + L_{q1L}I_{qL}. \quad (17)$$

For the simulation method detailed in this paper, it is required that (7) and (8) be rewritten in terms of inductances. To this end, (16) and (17) are substituted into (7) and (8), respectively. Thus, for set  $i = 1$  of the top layer, the  $dq$  voltage equations are

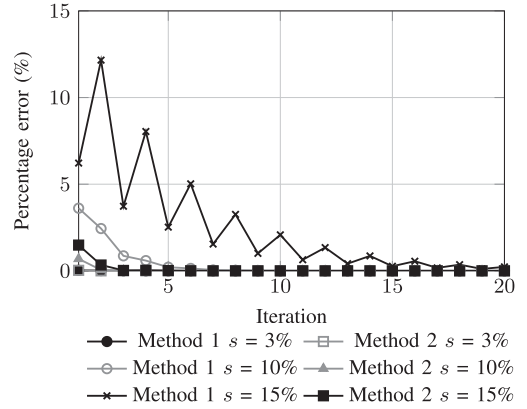


Fig. 7. Convergence rate using methods 1 and 2 for slip  $s = 3\%$ ,  $10\%$ , and  $15\%$ .

written as

$$0 = R_1 I_{dU} - \omega_{sle} L_{q1U} I_{qU} - \omega_{sle} L_{q1L} I_{qL} \quad (18)$$

$$0 = R_1 I_{qU} + \omega_{sle} L_{d1U} I_{dU} + \omega_{sle} L_{d1L} I_{dL} + \omega_{sle} \lambda_{m1}. \quad (19)$$

Since the bottom-layer flux linkage terms differ from the top-layer terms, it is required that (7) and (8) also be given for the bottom layer, in this case for set  $i = 2$ , as

$$0 = R_2 I_{dL} - \omega_{sle} L_{q2L} I_{qL} - \omega_{sle} L_{q2U} I_{qU} \quad (20)$$

$$0 = R_2 I_{qL} + \omega_{sle} L_{d2L} I_{dL} + \omega_{sle} L_{d2U} I_{dU} + \omega_{sle} \lambda_{m2} \quad (21)$$

where  $L_{d2L}$  and  $L_{d2U}$  of (21) and  $L_{q2L}$  and  $L_{q2U}$  of (20) are, respectively, the  $d$ -axis and  $q$ -axis inductances of bottom-layer coil set  $i = 2$ . It is worthwhile to note that  $L_{d1L}$  should equal  $L_{d2U}$  on the  $d$ -axis, and also  $L_{q1L}$  should equal  $L_{q2U}$  on the  $q$ -axis, since the mutual inductances between layers are the same.

To determine the four inductance terms of (18)–(21) and to solve then for the four currents from these equations becomes a bit complex. Thus, a simplification in (16) and (17) is proposed. To simplify (16), the assumption is made that  $I_{dL} \approx I_{dU}$ . Further with  $I_{dU} = I_{d1}$  from (12), (16) can be written as

$$\lambda_{d1} \approx L_{d1} I_{d1} + \lambda_{m1} \quad (22)$$

where  $L_{d1} = L_{d1U} + L_{d1L}$ , which is the total  $d$ -axis inductance of coil set  $i = 1$ . Applying this to the  $q$ -axis, by making the assumption that  $I_{qL} \approx I_{qU}$ , and with  $I_{qU} = I_{q1}$  from (13), (17) is simplified to

$$\lambda_{q1} \approx L_{q1} I_{q1} \quad (23)$$

where  $L_{q1} = L_{q1U} + L_{q1L}$ , which is the total  $q$ -axis inductance of coil set  $i = 1$ . The same simplification can be made for the bottom-layer coil sets, taking, e.g., coil set  $i = 2$ , which yields

$$\lambda_{d2} \approx L_{d2} I_{d2} + \lambda_{m2} \quad (24)$$

$$\lambda_{q2} \approx L_{q2} I_{q2}. \quad (25)$$

The assumption that the top and bottom-layer currents are equal is not correct (there is a percentage difference between these currents), but making this assumption enables a powerful

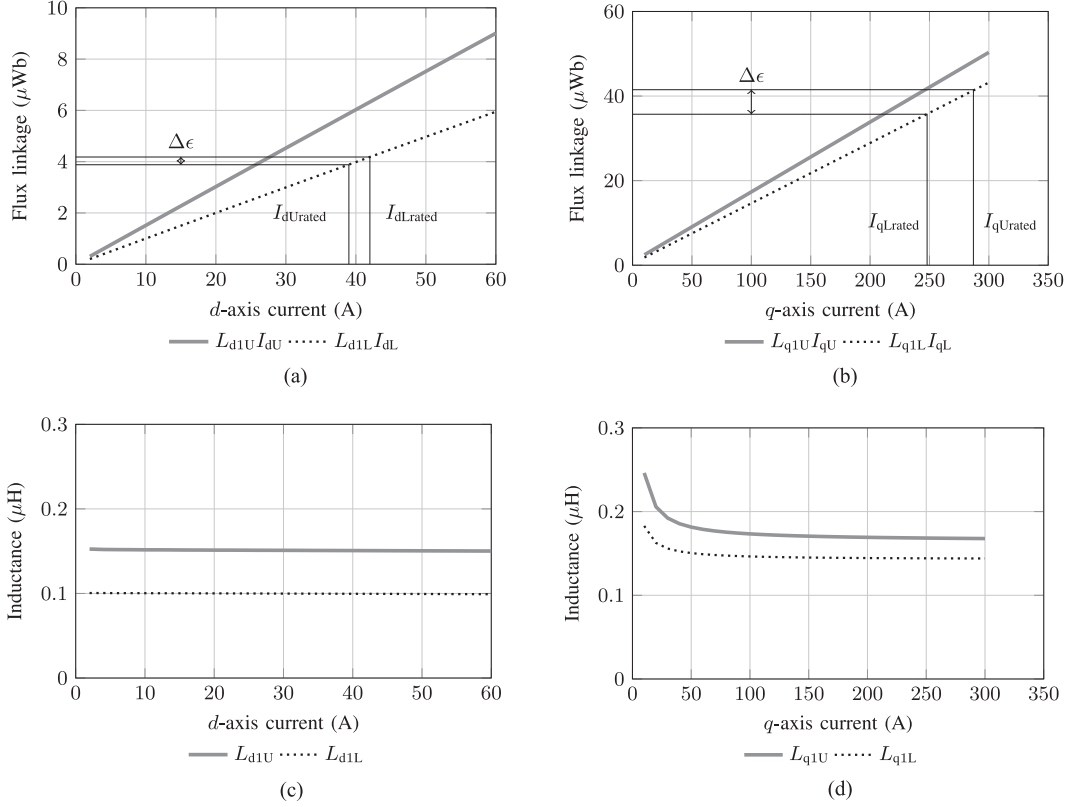


Fig. 8. Top-layer flux linkage terms versus (a)  $d$ -axis and (b)  $q$ -axis currents of coil winding set  $i = 1$ , and top-layer inductance terms versus (c)  $d$ -axis and (d)  $q$ -axis currents for the same coil set.

analysis method, which yields accurate results as are shown and explained in Sections VI and VII.

### C. Generic Equations

To allow the analysis of both the side-by-side and top-and-bottom layer configurations, a set of generic equations is developed which is applicable to both configurations. It is clear that (22) and (23) have the same format as (10) and (11), and accordingly generic equations for  $d$ - and  $q$ -axis flux linkage can be written as

$$\lambda_{di} = L_{di}I_{di} + \lambda_{mi} \quad (26)$$

$$\lambda_{qi} = L_{qi}I_{qi} \quad (27)$$

where  $L_{di}$  and  $L_{qi}$  are the  $d$ - and  $q$ -axis inductances and  $\lambda_{mi}$  is the PM flux linkage contribution for coil set  $i$ . Equations (26) and (27) can be written in terms of  $dq$  inductances as

$$L_{di} = \frac{\lambda_{di} - \lambda_{mi}}{I_{di}} \quad (28)$$

$$L_{qi} = \frac{\lambda_{qi}}{I_{qi}} \quad (29)$$

To determine  $\lambda_{di}$  and  $\lambda_{qi}$  of (26) and (27), given  $dq$  currents are transformed to

$$\mathbf{I}_{abc(i)} = \mathbf{K}_p^{-1}(\theta_i)\mathbf{I}_{dq(i)} \quad (30)$$

with

$$\theta_i = (i - 1)\delta \quad (31)$$

where  $\delta = \pi p/N_s$ , which is the electrical slot-pitch angle of the working harmonic.  $\mathbf{K}_p^{-1}$  is Park's inverse transformation. The phase currents of (30) are given as input to the FE software, from which the phase flux linkages ( $\lambda_{abc(i)}$ ) are obtained as an output. These flux linkages are then transformed back to the  $dq$  domain to determine  $\lambda_{di}$  and  $\lambda_{qi}$  of (26) and (27) as

$$\lambda_{dq(i)} = \mathbf{K}_p(\theta_i)\lambda_{abc(i)}. \quad (32)$$

With the  $dq$  flux linkages and  $dq$  currents known, the  $dq$  inductances of (28) and (29) can be determined (note  $\lambda_{mi}$  can be determined from the FE analysis at no load).

The simplified generic equations for flux linkage, as given by (26) and (27), allows for the simplification of (18)–(21). Using (26) and (27), (7) and (8) are rewritten in terms of  $L_{di}$ ,  $L_{qi}$ , and  $\lambda_{mi}$  as

$$0 = R_i I_{di} - \omega_{sle} L_{qi} I_{qi} \quad (33)$$

$$0 = R_i I_{qi} + \omega_{sle} L_{di} I_{di} + \omega_{sle} \lambda_{mi}. \quad (34)$$

All equations thus far are based on a two-dimensional (2-D) model. To take 3-D effects into account, the effects of end windings must be included. The end-winding resistance is already included in  $R_i$  of (33) and (34). A voltage term for end-winding inductance  $L_{ei}$  (calculated using a method in [15]) is added to

(33) and (34) as

$$0 = R_i I_{di} - \omega_{sle} L_{ei} I_{qi} - \omega_{sle} L_{qi} I_{qi} \quad (35)$$

$$0 = R_i I_{qi} + \omega_{sle} L_{ei} I_{di} + \omega_{sle} L_{di} I_{di} + \omega_{sle} \lambda_{mi}. \quad (36)$$

Furthermore, (35) and (36) are rewritten in terms of  $dq$ -axis current as

$$I_{di} = \frac{-\omega_{sle}^2 (L_{qi} + L_{ei}) \lambda_{mi}}{R_i^2 + \omega_{sle}^2 (L_{qi} + L_{ei})(L_{di} + L_{ei})} \quad (37)$$

$$I_{qi} = \frac{-\omega_{sle} R_i \lambda_{mi}}{R_i^2 + \omega_{sle}^2 (L_{qi} + L_{ei})(L_{di} + L_{ei})}. \quad (38)$$

The generated developed torque is calculated using

$$T = \frac{N_s}{S} \sum_{i=1}^{S/3} \frac{3}{2} \left( \frac{p}{2} \right) (\lambda_{di} I_{qi} - \lambda_{qi} I_{di}). \quad (39)$$

As the core, PM, and bearing losses of the coupler are practically zero at rated slip frequency and rated slip speed (4.2 Hz and 18 r/min, respectively, in this case), these losses, as well as the windage losses, are assumed to be zero. Hence, the only losses considered are the conductor losses, which are calculated as

$$P_{cu} = T \omega_{sl} = \frac{N_s}{S} \sum_{i=1}^{S/3} \frac{3}{2} I_i^2 R_i \quad (40)$$

where

$$I_i = \sqrt{I_{di}^2 + I_{qi}^2} \quad (41)$$

with  $I_i$  the peak phase current of coil set  $i$  and  $\omega_{sl}$  the mechanical slip speed in rad/s.

## VI. SOLVING COIL CURRENTS

Since the slip coupler operates on the principle of slip and induced currents, the coil currents are not known beforehand. Of course, transient FE simulations can be run at a certain slip speed to determine the steady-state coil currents, but this is too computationally expensive for a design optimization and steady-state simulation of the slip coupler.

A method is proposed whereby the static FE solutions together with equivalent circuit voltage equations are used to solve for the coil currents. Two methods are considered, of which one method directly makes use of (7) and (8), where voltage terms  $\omega_{sle} L_{ei} I_{qi}$  and  $\omega_{sle} L_{ei} I_{di}$  for end-winding inductance are added to (7) and (8), respectively. The second method makes use of (37) and (38). For both methods, the rated torque  $T_{rated}$ , slip  $s$ , and synchronous operating speed is known. Note that for a top-bottom layer configuration, the rotor coil resistance,  $R_i$ , will differ between the layers and must accordingly be taken into account. In the following sections, the two methods proposed for solving of the currents are explained.

### A. Method 1—Flux Linkage Method

The first method is used to calculate the coil currents iteratively from the information on flux linkages as follows.

- 1) Use, initially, the known  $T_{rated}$  and  $s$  to calculate  $P_{cu}$  from the first term in (40). Assuming equal conductor losses in

all the coil phases, calculate  $I_i$  using the summation term of (40).

- 2) Set initial starting values of  $dq$  currents as  $I_{qi} = I_i$  and  $I_{di} = 0$ . Transform the  $dq$  currents to the phase domain using (30). Using  $\mathbf{I}_{abc(i)}$  as input, run a first static FE solution to determine  $\lambda_{abc(i)}$ .

Steps 1 and 2 are always used to initialize. The following steps are used iteratively.

- 3)  $\lambda_{abc(i)}$  is transformed to  $dq$  flux linkages using (32), to get  $\lambda_{dq(i)}$  ( $\lambda_{di}$  and  $\lambda_{qi}$ ).
- 4) With  $\lambda_{di}$  and  $\lambda_{qi}$  known, calculate new values for  $I_{di}$  and  $I_{qi}$  at the required  $\omega_{sle}$  using (7) and (8).
- 5) Convert  $I_{di}$  and  $I_{qi}$  to the phase domain using (30), and run a next static FE solution to determine  $\lambda_{abc(i)}$ .
- 6) Go to step 3 and repeat until convergence of the currents.

### B. Method 2—Inductance Method

The second method is also used to calculate the coil currents iteratively, but this time based on information of  $L_{di}$ ,  $L_{qi}$ , and  $\lambda_{mi}$ .

- 1) Use, initially, the known  $T_{rated}$  and  $s$  to calculate  $P_{cu}$  from the first term in (40). Assuming equal conductor losses in all the coil phases, calculate  $I_i$  using the summation term of (40).
- 2) Set initial starting values of  $dq$  currents as  $I_{qi} = I_i$  and  $I_{di} = 0$ . Transform the  $dq$  currents to the phase domain using (30). Using  $\mathbf{I}_{abc(i)}$  as input, run a first static FE solution to determine  $\lambda_{abc(i)}$ .
- 3)  $\lambda_{abc(i)}$  is transformed to  $dq$  flux linkages using (32), to get  $\lambda_{dq(i)}$  ( $\lambda_{di}$  and  $\lambda_{qi}$ ).
- 4) With  $I_{di} = 0$ ,  $\lambda_{mi}$  is calculated from (26) with  $\lambda_{mi} = \lambda_{di}$ .
- 5)  $L_{qi}$  is calculated using (29), and  $L_{di} = L_{qi}$  as an initial estimate.

Steps 1–5 are always used to initialize. The following steps are used iteratively.

- 6) Calculate new values for  $I_{di}$  and  $I_{qi}$  at the required  $\omega_{sle}$  using (37) and (38). Transform to the phase domain using (30) and run a next FE solution to determine  $\lambda_{abc(i)}$ .
- 7)  $\lambda_{abc(i)}$  is transformed to  $dq$  values using (32).  $\lambda_{di}$  and  $\lambda_{qi}$  are used in (28) and (29) to calculate  $L_{di}$  and  $L_{qi}$  ( $\lambda_{mi}$  is calculated in step 4).
- 8) Test for convergence of the currents; if not, go to step 6 and repeat until convergence.

Both methods are used to determine the currents and flux linkages of the slip coupler at a given slip value. Note that both methods use two FE static solutions for the first iteration, but only one FE static solution per iteration thereafter. Hence, the solution time per iteration is very much the same for both methods. The methods are compared to determine which method requires the least number of FE solutions (or iterations) for convergence. The results for different slip values can be observed in Fig. 7. The final convergence value is identical in both methods, but the number of iterations until convergence differs greatly. Clearly, Method 2 converges much quicker, with almost all cases converging within four iterations. Method 1 generally requires more iterations, especially at higher slip values. Hence,

Method 2 is recommended for use in the design optimization of the slip coupler or for steady-state simulation.

## VII. INDUCTANCES OF TOP-BOTTOM COIL WINDING

The inductances of the top-bottom coil winding configuration are investigated to determine the amount of mutual coupling between the various phase coils and layers, as well as to investigate the effects of the simplifications made in (22) and (23). The  $d$ -axis inductance for set  $i = 1$  is investigated by considering the various components of (16) and calculating the various flux linkage terms individually. From these flux linkage terms, the individual self- and mutual inductance terms can be determined.

The inductance contribution from the top-layer windings,  $L_{d1U}$ , is determined by setting  $I_{dL}, I_{qU}, I_{qL} = 0$ , and running a set of the static FE solutions for  $I_{dU} = 0-60$  A (60 A is about 1.5 p.u. current). The term  $\lambda_{m1}$  of (16) is determined with  $I_{dU} = 0$  (i.e., all the currents are zero). For  $I_{dU} \neq 0$ , the inductance  $L_{d1U}$  is determined from (16) as

$$L_{d1U} = (\lambda_{d1} - \lambda_{m1})/I_{dU} \quad \{I_{dL} = 0 \text{ A}\}. \quad (42)$$

The mutual inductance contribution from the bottom-layer coil windings,  $L_{d1L}$ , is also determined, but this time by setting  $I_{dU}, I_{qU}, I_{qL} = 0$ , and again running a set of the static FE solutions for  $I_{dL} = 0-60$  A. This inductance is calculated from (16) as

$$L_{d1L} = (\lambda_{d1} - \lambda_{m1})/I_{dL} \quad \{I_{dU} = 0 \text{ A}\} \quad (43)$$

for each solution. The results of these calculations are shown in Fig. 8(a) for the flux linkage terms, and in Fig. 8(c) for the inductance terms. This procedure is repeated to determine the  $q$ -axis inductances using (17) and running the static FE solutions for  $I_{qU}$  and  $I_{qL}$  between 0–300 A (300 A is about 1.2 p.u. current). The results of these calculations are shown in Fig. 8(b) for the flux linkage terms  $L_{q1U}I_{qU}$  and  $L_{q1L}I_{qL}$  and in Fig. 8(d) for the inductance terms  $L_{q1U}$  and  $L_{q1L}$ .

From Fig. 8(c) and (d), it can be seen that the mutual inductances from the bottom-layer coil windings contribute to a large percentage ( $\approx 40\%$ ) of the total inductance. The  $q$ -axis inductance is higher than the  $d$ -axis inductance of the top-layer winding, thus some saliency is present due to the difference in saturation levels of the  $d$ -axis and  $q$ -axis. The effects of the simplifications made in (22) and (23) are illustrated in Fig. 8(a) and (b). In Fig. 8(a), the rated  $I_{dU}$  and  $I_{dL}$  currents (as determined by Method 1 with no simplifications) are shown, as well as the corresponding flux linkage values for  $L_{d1L}I_{dL}$ , with the difference indicated by  $\Delta\epsilon$ . This difference  $\Delta\epsilon$  is the error which is made using the simplification of (22). This error is found to be 0.04% of the total  $d$ -axis flux linkage, bearing in mind that the vast majority of  $d$ -axis flux linkage is due to the PMs. Similarly for the  $q$ -axis, the error due to the simplification of (23) is shown in Fig. 8(b). In this case,  $\Delta\epsilon$  is found to be 6% of the total  $q$ -axis flux linkage. This is considerably more than the  $d$ -axis error, but is still a very small portion (0.7%) of the total phase flux linkage. Thus, the simplifications made in (22) and (23) appear to have a negligible effect.

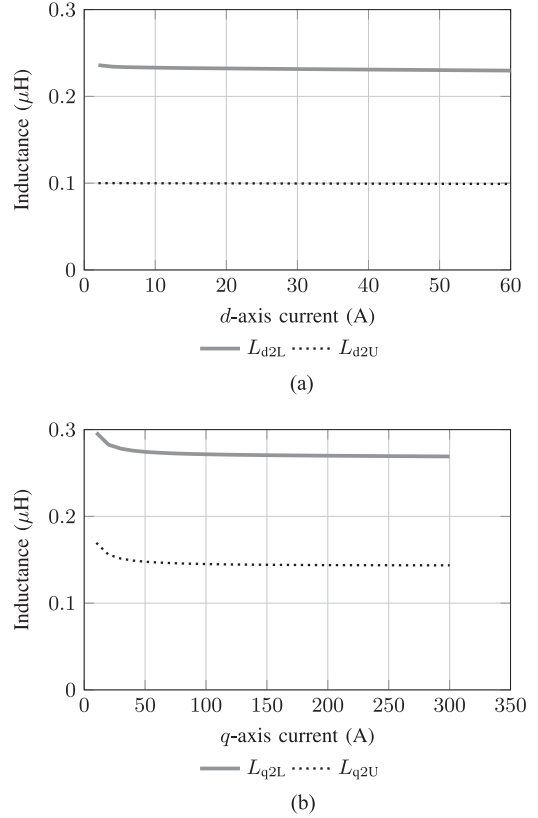


Fig. 9. Bottom-layer inductance terms versus (a)  $d$ -axis and (b)  $q$ -axis currents for coil winding set  $i = 2$ .

The above procedure is repeated to determine the inductances of the bottom-layer coil set  $i = 2$ . The  $d$ -axis inductances  $L_{d2L}$  and  $L_{d2U}$  are shown in Fig. 9(a) and the  $q$ -axis inductances  $L_{q2L}$  and  $L_{q2U}$  in Fig. 9(b). Comparing the  $dq$  inductances of the bottom-layer coil winding of Fig. 9 with that of the top-layer coil winding of Fig. 8(c) and (d), it can be seen that the mutual inductance terms of both layers are the same, which is correct, but that the total self-inductances of the bottom-layer coil winding are more than 50% higher than that of the top-layer coil winding. This is due to the fact that the bottom-layer coils are deeper inside the rotor slots. The coil impedance of the bottom-layer winding is thus much higher, giving further indication that the bottom-layer short-circuited coils will have lower induced currents than that of the top-layer short-circuited coils, specifically at higher slip frequencies.

## VIII. DESIGN OPTIMIZATION

The design optimization of the slip coupler is performed using Method 2 as described in Section VI. In the design optimization, the FE solutions are combined with the *VisualDoc* optimization suite[17]. In the static FE solutions, the slip coupler is time stepped through one electrical period to allow for the evaluation of the torque ripple. The required torque ( $T_{\text{rated}}$ ) in the optimization of the slip coupler is 42 N·m. A single objective design optimization is done by minimizing the active mass of the slip coupler, subject to various constraints. The optimized variables and constraints used in the slip coupler design, with geometry

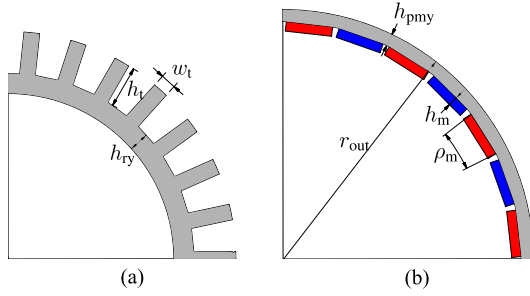


Fig. 10. Coupler dimensions used as optimization input variables [16].

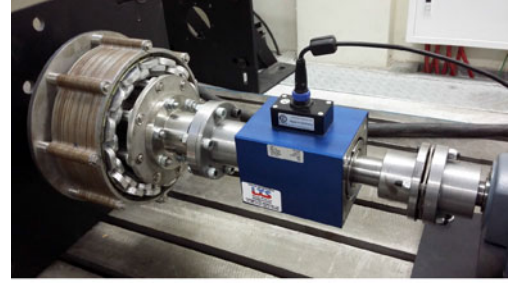
TABLE I  
SPECIFICATIONS, OPTIMIZATION VARIABLES AND OPTIMIZED VALUES FOR SLIP COUPLER

General Specifications	Value
Rated Output Speed	600 r/min
Number of Poles	28
Number of Slots	30
Magnet Type and Grade	NdFeB N48H
Fixed Dimensions	Value
Inner Diameter	147 mm
Airgap	1.5 mm
Optimization Variables	Optimized Value
Axial Length	65 mm
Tooth Height - $h_t$	17.3 mm
Tooth Width - $w_t$	6.4 mm
Coil Height	7.5 mm
Wound Rotor Yoke - $h_{ry}$	8 mm
Magnet Height - $h_m$	4 mm
Magnet Pitch - $\rho_m$	87%
PM Rotor Yoke - $h_{pmy}$	5 mm
Outer Diameter - $r_{out}$	210 mm
Objective Function	Optimized Value
Active Mass	7 kg
Constraint (at rated slip)	Value
Generated Torque	$41 < T < 43$ Nm
Torque Ripple	$< 3\%$
Efficiency	$= 97\%$
Current Density	$< 4$ A/mm <sup>2</sup>

TABLE II  
TYPICAL INDUCTANCE AND RESISTANCE VALUES OF SLIP COUPLER

	Top	Bottom
Resistance ( $R_i$ ) at 45°C	69 $\mu\Omega$	79 $\mu\Omega$
Resistance ( $R_i$ ) at 75°C	78 $\mu\Omega$	88 $\mu\Omega$
$d$ -Axis Inductance ( $L_{di}$ )	251 nH	335 nH
$q$ -Axis Inductance ( $L_{qi}$ )	347 nH	493 nH

and dimensions as shown in Figs. 1 and 10 are given in Table I. The resistance and inductance values of the slip coupler are given in Table II.



(a)



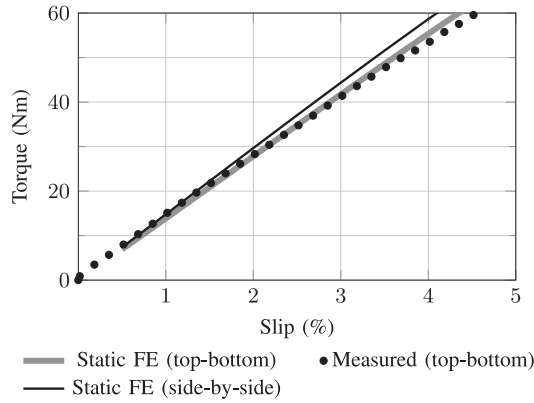
(b)

Fig. 11. (a) Test setup used for the slip coupler prototype and (b) aluminum coil ends.

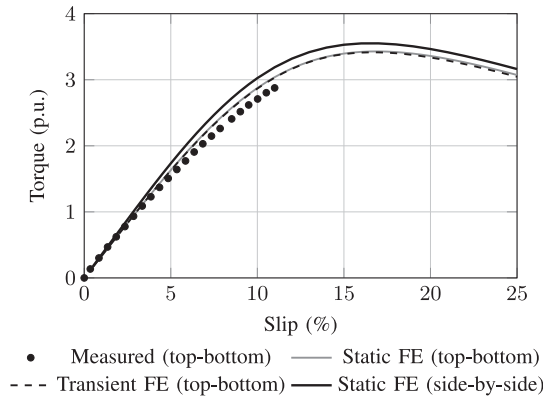
## IX. CALCULATED AND MEASURED RESULTS

A prototype of the optimized top–bottom layer configuration slip coupler, as detailed in Table I, was constructed and tested. The slip coupler prototype is shown in Fig. 11(a) with a close-up view of the stacked aluminum plate coils shown in Fig. 11(b). For testing the coupler, the mechanical output of the coupler is fixed to the test bench and a Lorentz torque and speed sensor is connected to the input to measure the input torque and speed of the coupler as shown in Fig. 11(a). A variable speed induction motor drive with a 1 : 50 reduction gear box is used to vary the slip speed and, hence, the torque of the coupler. The measured test results are compared with the calculated results obtained using the proposed static FE analysis method. The measured and static FE results are also compared with transient FE simulation results. For the 2-D static FE calculations, a non-commercial package called *SEMFEM* [18] was used, while for the 2-D transient FE calculations the package *Infolytica MagNet* was used.

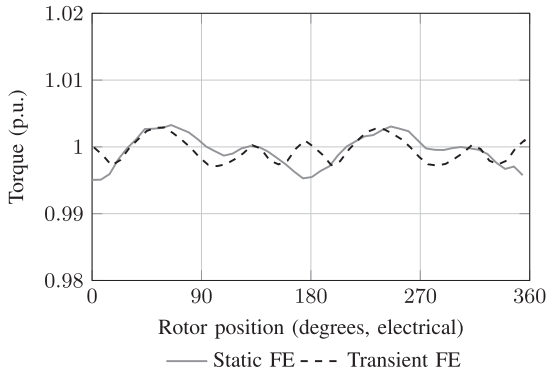
The results of torque versus slip of the prototype slip coupler are shown in Fig. 12(a). These results show that there is very good agreement between measurements and static FE calculations. Temperature measurements of the short-circuited coil ends were also conducted during the tests using a thermal imaging camera. The average of these measured temperatures was used in the calculation of the short-circuited coil resistances, which greatly affects the torque–slip performance of the coupler. With the slip coupler operating at its rated output speed (600 r/min) and rated load a fairly cold average coil temperature of 45 °C was measured, which indicates the effective cooling of



(a)



(b)

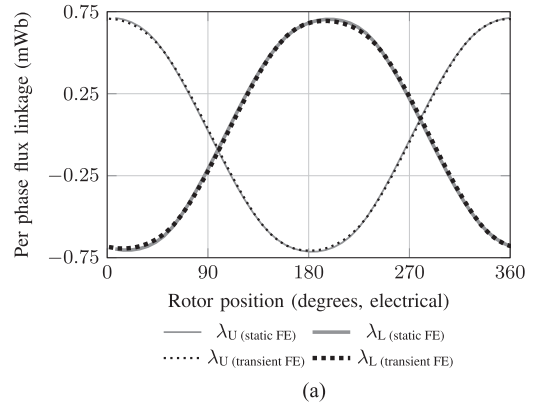


(c)

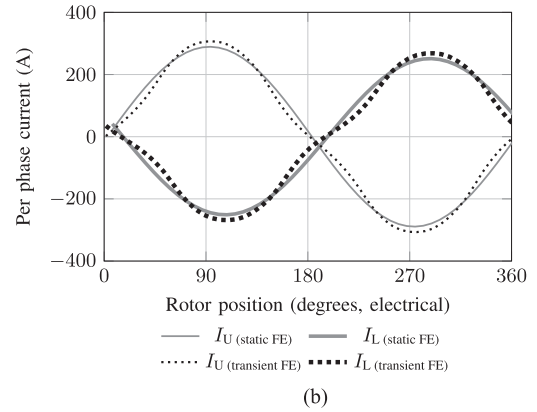
Fig. 12. (a) Average torque versus slip, (b) average torque versus slip characteristic over a wide slip range and (c) torque versus rotor position at rated slip ( $s = 3\%$ ) of the slip coupler.

the slip coupler with its rotating coil ends in direct contact with the cold ambient air.

In Fig. 12(a), the calculated torque versus slip of the side-by-side winding machine of Fig. 1(a) is also shown. In this calculation, the proposed top-bottom layer analysis was used again with each side-by-side coil divided in this case into two coils, a top coil and a bottom coil. It is shown in Fig. 12(a) that the side-by-side winding machine develops a slightly higher torque (6% higher at rated slip) than the top-bottom winding machine. It is important to note that the conductor cross-sectional area



(a)



(b)

Fig. 13. Upper and lower layer (a) coil flux linkage and (b) coil current waveforms of the slip coupler according to transient and time-stepped static FE simulations at rated slip ( $s = 3\%$ ).

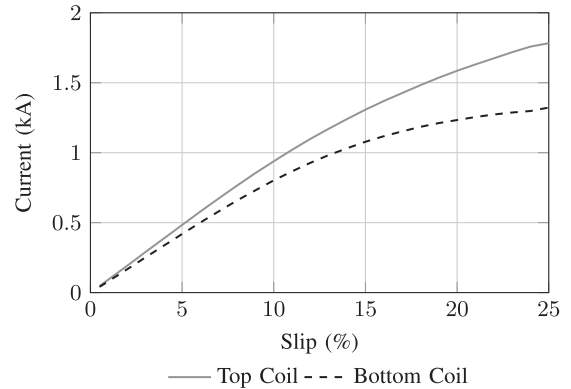


Fig. 14. Peak phase current ( $I_i$ ) versus slip, indicating the difference in current between top- and bottom-layer coils.

per slot of the side-by-side winding is the same as that of the top-bottom winding, but the end winding length of the side-by-side winding is shorter. The increase in torque is thus due to the lower end winding resistance of the side-by-side winding that leads to a higher induced current and higher torque. This result emphasizes the advantage of the side-by-side winding.

In Fig. 12(b), the average torque of the static FE and transient FE simulations of the slip coupler over a wide slip range of 0%–25% are shown. The measured results of Fig. 12(a) are also

shown on this graph. The results show the high accuracy of the proposed static FE analysis method for up to large percentages of slip. Note also from this figure the high pull-out torque of 3.4 p.u. of the prototype slip coupler.

The simulated torque waveforms versus rotor position of the static FE and transient FE analysis methods are compared in Fig. 12(c). This shows a slight difference in the results from these methods, which is expected from the fact that the FE software packages and meshes used differ. Nevertheless, the torque ripple percentages according to the two methods are in close agreement. The torque ripple of this coupler is also seen to be very small, which is to be expected from a 28/30 pole/slot combination.

The flux linkage and current waveforms of the short-circuited coils are also compared between the static and transient FE simulations. As can be seen in Fig. 13, the flux linkage and current waveforms match quite closely, i.e., for both the top- and bottom-layer coils at the full-load slip of  $s = 3\%$ . Note from the transient FE solution in Fig. 13(b) that there is a small third harmonic current (zero-sequence component current) that flows in the coil. Zero-sequence component coil currents can flow as the short-circuited phase coils are not star-connected but separate. Note further from Fig. 13(b), the clear difference (15%) in the current magnitudes of the top- and bottom-layer coils. The difference in top-and-bottom coil currents is further highlighted in Fig. 14. Here the effect of higher slip frequency is very clear, with a 34% difference in the coil currents at a slip of 25% (35 Hz slip frequency).

## X. CONCLUSION

In this paper, the analysis of PM slip couplers with side-by-side or top-bottom short-circuited nonoverlap coil windings is considered. From the analysis and the results, the following conclusions are drawn.

- 1) It is shown by multi three-phase MMF theory that individual side-by-side or top-bottom nonoverlap tooth coils of valid three-phase pole-slot combination machines can be short circuited for correct PM slip coupler operation. The theory also shows that the MMF harmonic content of these short-circuited coil windings is relatively low with almost no sub working-harmonic MMFs.
- 2) The method proposed for the fast calculation of the steady-state short-circuited coil currents and the torque of the slip coupler is found to be very accurate compared to transient FE analysis results over a relatively large slip range of the machine. The accuracy was specifically found for top-bottom short-circuited coils where the RMS coil currents differ. Using a number of static FE solutions, the method takes the effects of saturation, saliency, and the mutual coupling between the coils and layers correctly into account. This all makes the method particularly attractive to be used in the design optimization of the PM coupler.
- 3) However, looking critically at the proposed method, it must be noted that the calculation of the coil flux linkage due to the PMs,  $\lambda_{mi}$ , is not entirely correct as this is not done at the absolute correct saturation levels of the machine. With accurate results found, however, it is con-

cluded that this approximation is valid in the calculation of the coil currents.

- 4) It is found that the RMS currents in the top- and bottom-layer coils of the PM coupler prototype differ by 15% at rated slip, but as much as 24% at maximum torque. Hence, it is incorrect to assume in the analysis that these currents are the same. The difference in the currents is explained by the difference in the impedances of the top and bottom coils; inductance calculations in the paper reveal that the bottom coil inductances are as much as 50% higher than that of the top coil inductances.
- 5) The side-by-side winding has the advantage that the end winding resistance is less than that of the top-bottom winding leading to a higher induced current and higher developed torque. This increase in torque by the side-by-side winding machine was found to be 6% at rated slip for the coupler investigated.

## REFERENCES

- [1] M. H. Nagrial, J. Rizk, and A. Hellany, "Design and development of magnetic torque couplers and magnetic gears," in *Proc. IEEE Int. Conf. Elect. Eng.*, Lahore, Pakistan, Apr. 2007, pp. 1–5.
- [2] Z. Meng, Z. Zhu, and Y. Sun, "3-D analysis for the torque of permanent magnet coupler," *IEEE Trans. Magn.*, vol. 51, no. 4, Apr. 2015, Art. 8002008.
- [3] R. You, J. Chai, X. Sun, and Y. Lin, "Variable speed wind turbine based on electromagnetic coupler and its experimental measurement," in *Proc. PES General Meeting, Conf. Expo.*, National Harbour, MD, USA, Jul. 2014, pp. 1–5.
- [4] S. Mohammadi, M. Mirsalim, and S. Vaez-Zadeh, "Nonlinear modeling of eddy-current couplers," *IEEE Trans. Energy Convers.*, vol. 29, no. 1, pp. 224–231, Mar. 2014.
- [5] J. Wang, H. Lin, S. Fang, and Y. Huang, "A general analytical model of permanent magnet eddy current couplings," *IEEE Trans. Magn.*, vol. 50, no. 1, 2014, Art. 8000109.
- [6] J. H. Potgieter and M. J. Kamper, "Design of new concept direct grid-connected slip-synchronous permanent-magnet wind generator," *IEEE Trans. Ind. Appl.*, vol. 48, no. 3, pp. 913–922, May 2012.
- [7] S. You, S. Wang, M. Tsai, and S. Mao, "Characteristic analysis of slotted-type axial-flux permanent magnetic couplers," in *Proc. IEEE Int. Conf. Elect. Mach. Syst.*, Sapporo, Japan, Oct. 2012, pp. 1–5.
- [8] J. H. Potgieter and M. J. Kamper, "Optimum design and comparison of slip permanent-magnet couplings with wind energy as case study application," *IEEE Trans. Ind. Appl.*, vol. 50, no. 5, pp. 3223–3234, Sep. 2014.
- [9] P. J. J. Van Wyk and M. J. Kamper, "Simplified analysis technique for double layer non-overlap multiphase slip permanent magnet couplings in wind energy applications," in *Proc. IEEE Int. Elect. Mach. Drives Conf., Coeur D'Alene, ID, USA, May 2015*, pp. 1317–1323.
- [10] E. Levi, R. Bojoi, F. Profumo, H. Toliyat, and S. Williamson, "Multiphase induction motor drives—A technology status review," *IET Elect. Power Appl.*, vol. 1, no. 4, pp. 489–516, 2007.
- [11] G. Renukadevi and K. Rajambal, "Generalized model of multi-phase induction motor drive using MATLAB/simulink," in *Proc. IEEE PES Innovative Smart Grid Technol.—India*, Kerala, India, Dec. 2011, pp. 114–119.
- [12] A. J. Rix, "Design, comparison and experimental evaluation of non-overlap winding radial flux permanent magnet hub drives for electric vehicles," Ph.D. dissertation (Chapter 2), Dept. of Elect. and Electron. Eng., Stellenbosch University, Stellenbosch, South Africa, Mar. 2011.
- [13] M. V. Cistelean, F. J. T. E. Ferreira, and M. Popescu, "Three phase tooth-concentrated multiple-layer fractional windings with low space harmonic content," in *Proc. IEEE Energy Convers. Congr. Expo.*, Atlanta, GA, USA, Sep. 2010, pp. 1399–1405.
- [14] E. Fornasiero, L. Alberti, N. Bianchi, and S. Bolognani, "Considerations on selecting fractional-slot windings," in *Proc. IEEE Energy Convers. Congr. Expo.*, Atlanta, GA, USA, Sep. 2010, pp. 1376–1383.
- [15] J. H. J. Potgieter and M. J. Kamper, "Calculation methods and effects of end-winding inductance and permanent-magnet end flux on performance prediction of nonoverlap winding permanent-magnet machines," *IEEE Trans. Ind. Appl.*, vol. 50, no. 4, pp. 2458–2466, Jul. 2014.

- [16] P. J. J. Van Wyk, "Design and evaluation of medium speed geared direct grid-connected wind generator drive train with specific focus on slip permanent magnet coupling," M.Sc. thesis, Dept. Elect. and Electron. Eng., Stellenbosch Univ., Stellenbosch, South Africa, 2015. [Online]. Available: <http://hdl.handle.net/10019.1/97889>
- [17] *VisualDOC Users Manual*, 6th ed., Vanderplaats Res. Develop., Inc., Colorado Springs, CO, USA, 2006.
- [18] S. Gerber, "A finite element based optimisation tool for electrical machines," M.Sc. thesis, Dept. of Elect. and Electron. Eng., Stellenbosch Univ., Stellenbosch, South Africa, 2011. [Online]. Available: <http://hdl.handle.net/10019.1/6635>



**Petrus J. J. van Wyk** (S'15) received the B.Eng. degree in 2011 and the M.Eng. degree in electrical engineering in 2015, both from the University of Stellenbosch, Stellenbosch, South Africa.

His current research interests include design and optimization of permanent magnet and induction machines, with specific focus on electromagnetic couplings.



**Maarten J. Kamper** (SM'08) received the M.Sc. (Eng.) degree in 1987 and the Ph.D. (Eng.) degree in 1996, both from the University of Stellenbosch, Stellenbosch, South Africa.

He has been with the academic staff of the Department of Electrical and Electronic Engineering, University of Stellenbosch, since 1989, where he is currently a Professor of electrical machines and drives. His research interests include computer-aided design and control of reluctance, permanent magnet, and induction machine drives.

Prof. Kamper is a South African National Research Foundation Supported Scientist and a Registered Professional Engineer in South Africa.